



Self-starting VCSEL-based optical frequency comb generator

Christian Daniel Muñoz-Arcos, Margarita Varón-Durán, Fabien Destic, Angélique Rissons

► To cite this version:

Christian Daniel Muñoz-Arcos, Margarita Varón-Durán, Fabien Destic, Angélique Rissons. Self-starting VCSEL-based optical frequency comb generator. Optics Express, 2020, 28 (3), pp.34860-34874. 10.1364/OE.400970 . hal-02988095

HAL Id: hal-02988095

<https://hal.science/hal-02988095>

Submitted on 4 Nov 2020

HAL is a multi-disciplinary open access archive for the deposit and dissemination of scientific research documents, whether they are published or not. The documents may come from teaching and research institutions in France or abroad, or from public or private research centers.

L'archive ouverte pluridisciplinaire **HAL**, est destinée au dépôt et à la diffusion de documents scientifiques de niveau recherche, publiés ou non, émanant des établissements d'enseignement et de recherche français ou étrangers, des laboratoires publics ou privés.



Open Archive Toulouse Archive Ouverte (OATAO)

OATAO is an open access repository that collects the work of some Toulouse researchers and makes it freely available over the web where possible.

This is a publisher's version published in: <https://oatao.univ-toulouse.fr/26877>

Official URL : <https://doi.org/10.1364/OE.400970>

To cite this version :

Muñoz-Arcos, Christian Daniel and Varón-Durán, Margarita and Destic, Fabien and Rissons, Angélique Self-starting VCSEL-based optical frequency comb generator. (2020) Optics Express, 28 (3). 34860-34874. ISSN 1094-4087

Any correspondence concerning this service should be sent to the repository administrator:

tech-oatao@listes-diff.inp-toulouse.fr



Self-starting VCSEL-based optical frequency comb generator

CHRISTIAN DANIEL MUÑOZ,^{1,2,*}  MARGARITA VARÓN,²  FABIEN DESTIC,¹  AND ANGÉLIQUE RISSONS¹ 

¹ISAE-SUPAERO, Université de Toulouse, Toulouse 31055, France

²CMUN Research Group, Universidad Nacional de Colombia, Bogotá 111321, Colombia

*chdmunoz@unal.edu.co

Abstract: In this paper, we present the simulation and experimental results of the first closed-loop system based on a directly modulated VCSEL in a gain-switching condition to generate optical frequency combs (OFC). In order to simulate the self-starting VCSEL-based optical frequency comb generator (SVOFC), we applied an intrinsic parameter extraction process to a C-band VCSEL using laser rate equations, static and dynamic measurements, and equivalent circuit models. The widest (62 GHz) and flattest (0.8) simulated OFC is obtained when the repetition frequency f_0 is 2.5 GHz. Implementation of the C-band SVOFC also shows that under constant electrical conditions, flatness higher than 0.85 and spectral widths of 50 GHz are obtained when $f_0 = 2.5$ GHz. The lowest phase noise at 10 kHz from the extracted electrical carrier is -127 dBc/Hz and is obtained when the optical fiber length is 5 km and $f_0 = 1.25$ GHz.

© 2020 Optical Society of America under the terms of the [OSA Open Access Publishing Agreement](#)

1. Introduction

Over the last few years, optical frequency comb (OFC) generation has emerged as a research topic of particular interest with a wide variety of applications such as spectroscopy [1,2], THz generation [3], LIDAR [4], optical communications [5], and physical variable sensing [6]. Additionally, the gain-switching (GS) technique has received special attention over other OFC generation techniques (e.g., mode-locking [7] and electro-optic modulation [8]) owing to its high flexibility, easy implementation, and low losses [9]. Frequency combs generated through GS of semiconductor lasers are characterized by high efficiency, high correlation between modes, and good tunability characteristics [10]. The GS technique consists of large-signal modulation of a semiconductor laser at a specific repetition frequency to ensure that only the first spike of the transient relaxation oscillations is excited [11]. Although edge-emitting lasers such as distributed feedback (DFB) [12] and discrete mode lasers (DML) [13] are preferred for their large modulation bandwidths, vertical-cavity surface-emitting lasers (VCSELs) have also been used for gain-switched OFC generation owing to their low threshold currents, low cost and single-mode transverse emission [14]. VCSEL-based OFCs produce energy-efficient and high mode coherence combs [15]. Also, two linear polarized OFCs in orthogonal directions can be produced using one gain-switched VCSEL under specific temperature and bias conditions [16,17].

Short-wavelength (SW) VCSELs are the dominant technology in data centers [18] (board interconnection) due to their mature manufacturing processes and high bit rates achieved at wavelengths from 850 nm to 980 nm [19,20]. Nevertheless, the capacity and link reach is limited by transmission losses and dispersion effects (chromatic and modal) in the optical fiber. Therefore, single-mode long-wavelength (LW) VCSELs, emitting in the range from 1260 nm to 1675 nm, are used today for short and long-reach interconnections applying different modulation formats to perform bit rates up to 100 Gb/s [21]. In the '90s, GS was applied to SW-VCSELs for optical pulse generation, and pulse durations of 19 ps and 24 ps were obtained at repetition frequencies of 0.5 GHz [22] and 8 GHz [23], respectively. Likewise, LW-VCSELs have been

widely used for short pulse generation [24] through GS and pulse timing jitter reduction using optical injection (OI) [25].

The OFC generation through closed optoelectronic loops has been widely investigated during the last decade. This mechanism has two features: the absence of external microwave signal generators and the presence of one or more cascade external modulators, which allow the generation of flat optical combs and sometimes, adjustable frequency spacing. In [26], the authors demonstrate an OFC generator based on an intensity modulator to generate a self-sustained microwave signal and a cascade phase modulator employed to enhance the number of comb tones. Optical combs with a flatness of 0.89 and 0.93 were generated at frequencies spaced 10 GHz and 12 GHz, respectively. A more complex implementation described in [27] includes an integrated dual-polarization dual-parallel Mach-Zehnder modulator (DP-DPMZM) to perform an up-conversion process. To up-convert an intermediate signal (IF) to different frequency bands, the OFC generated from an optoelectronic oscillator (OEO), and the first DPMZM is beaten in a photodetector with the optical-modulated intermediate frequency signal from the second DPMZM. An OFC with a spectral width of ~ 0.5 nm and seven optical tones separated at 10.8 GHz was generated. Other implementations replace the electrical filter of conventional OEOs with an optical filter using the frequency shift produced by stimulated Brillouin scattering (SBS) in an optical fiber [28,29]. The two proposed architectures yield an OFC with seven and nine tones at a frequency spacing of 10.89 GHz and 10.87 GHz, respectively.

In this article, we present the first self-starting closed-loop system for OFC generation based on an LW-VCSEL in GS condition. Unlike the systems with gain-switched VCSELs available in the literature, our system called self-started VCSEL-based optical frequency comb generator (SVOFC) does not require an electrical microwave reference signal. On the contrary, it can generate a low phase noise signal provided by the quality factor of the optical resonant cavity used. Furthermore, compared to closed-loop systems for OFC generation, the SVOFC exhibits a straightforward architecture because it does not incorporate any external optical modulation mechanism and includes a single amplification stage in the electrical domain.

In order to validate our system's performance, we propose a closed-loop simulation using a software tool. This type of simulation is not widely presented in the literature, and in many cases, the behavior of the components is assumed to be ideal. To obtain a better approximation of the real behavior of the VCSEL in GS condition, we performed an intrinsic laser parameter extraction. Some extraction procedures are based on measurements of the optical spectrum of the lasers operated in continuous-wave mode [30,31], AC small-signal response above threshold [32], and equivalent circuit models [33]. The model used in our work is based on the procedure proposed by Bacou *et al.* [34] for LW-VCSELs using dynamic measurements and an electrical model of the active region. Our procedure includes an electrical model of the electrical access, including wire bondings and TO package leads.

The paper is structured as follows. In Section 2 we present the architecture of a self-starting system for optical frequency comb generation called SVOFC. The rate equations for a single-mode VCSEL and the equivalent circuit model of the active region are presented in Section 3. In this section, the intrinsic parameter extraction of a C-band VCSEL is described and the extracted parameters are used to simulate the SVOFC generator in VPIphotonics Design SuitTM. In Section 4 the experimental OFCs are compared in terms of their flatness and spectral width, and the phase noise measurements of the electrical carrier are presented when O and C-band VCSELs are used. Finally, we will provide some conclusions to our work.

2. SVOFC principle and architecture

The self-started VCSEL-based optical frequency comb generator (SVOFC) allows optical pulse generation at a repetition frequency f_0 through a closed-loop self-starting system. The resonant cavity system consists of a single-mode optical fiber (acting as a Fabry-Perot resonator) with

length L , quality factor $Q = \pi \cdot f_0 / FSR$, and free-spectral range $FSR = c / (n_f \cdot L)$ (n_f refractive index). The noise provided by the components initiates the self-sustained oscillation. The optical pulses are generated by direct modulation of a VCSEL in gain-switching condition. The spectral purity of the modulating signal, which can be extracted from the loop just before modulating the VCSEL, is influenced by the quality factor of the resonant cavity.

In the time domain, the optical output of the SVOFC consists of optical pulses with amplitude A_p and full-width at half-maximum FWHM. The same optical output in the frequency domain corresponds to an optical frequency comb (OFC) characterized by the envelope flatness (defined as the ratio of total tones at 10 dB to total tones at 20 dB) and the 10 dB and 20 dB spectral widths, Δf_{10} and Δf_{20} respectively. The optical characteristics of the OFC depend on the fundamental frequency f_0 , the driving signal power, and the bias current of the VCSEL. In [35], the authors demonstrate that high-quality OFCs can be obtained at high bias currents and large driving signal amplitudes. Simultaneously, they proved that the smallest amplitude at which wide OFCs can be generated occurs when the f_0 frequency is close to the laser's resonance frequency f_R (related to the bias current). In the time domain, an OFC consists of an optical pulse train with a repetition frequency f_0 and physical characteristics influenced by the electrical conditions of the GS regime. For example, the pulse duration (FWHM) can be reduced when only the first spike of the transient laser relaxation response is excited by using a f_0 frequency higher than the transient response frequency [36].

The architecture of the SVOFC is shown in Fig. 1. The VCSEL optical output is connected to an optical isolator to avoid back reflections. The optical pulses are extracted by one arm of a variable ratio optical coupler (VROC) and reinjected into the system by the other arm. Then, the optical pulses are photodetected and microwave harmonics are generated at frequencies multiples of f_0 . The fundamental frequency harmonic is amplified through a microwave amplifier and filtered by a band-pass filter centered at f_0 . Finally, the loop is closed with the microwave signal by modulating the VCSEL directly through a bias-tee. The modulating electrical signal can be extracted via an electrical coupler (EC). An electrical attenuator is included to ensure the loop gain and the gain-switching condition. The floor phase noise of the fundamental frequency is governed by the amplifier white noise and can be reduced by adjusting the amplifier input power through the VROC ratio.

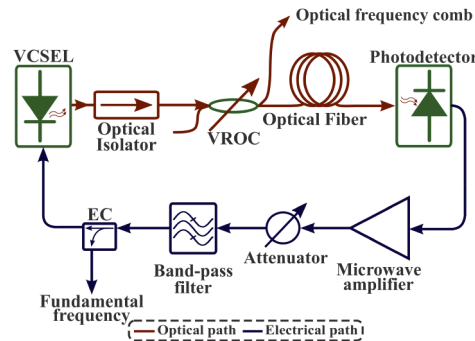


Fig. 1. Self-started VCSEL-based optical frequency comb generator architecture.

3. Parameter extraction and SVOFC simulations

In order to validate the performance of the SVOFC architecture, the closed-loop is simulated using computer-aided design (CAD) software. Considering that the OFC behavior depends on the physical characteristics of the VCSEL, the intrinsic parameters extraction is essential to obtain more reliable results. Both the extraction process and the simulation results are described below.

3.1. VCSEL parameter extraction

For this work, we use a C-band VCSEL manufactured by the Korean company RayCan. The active region consists of seven pairs of InAlGaAs quantum wells and a tunnel junction for reducing absorption losses [37]. To achieve high reflectivity into the cavity, two distributed Bragg reflectors (DBR) are included [38]. The VCSEL is mounted inside a TO-56 package and its output beam is coupled to a single-mode optical fiber.

The static and dynamic characteristics of directly modulated VCSELs can be obtained using a temperature-independent single-mode rate equation model composed of three differential equations: carrier density $N(t)$ (electrons or holes), photon density $S(t)$, and optical phase $\phi(t)$. The rate equations for a single-mode VCSEL are as follow [39]:

$$\frac{dN(t)}{dt} = \frac{\eta_i I(t)}{qV_{act}} - \left(A + BN(t) + CN^2(t) \right) N(t) - v_g GS(t) \quad (1)$$

$$\frac{dS(t)}{dt} = \Gamma \beta BN^2(t) + \Gamma v_g GS(t) - \frac{S(t)}{\tau_p} \quad (2)$$

$$\frac{d\phi(t)}{dt} = \frac{\alpha_H \Gamma v_g a_0}{2} (N(t) - N_{tr}), \quad (3)$$

where η_i is the internal quantum efficiency, I the injected current into the cavity, q the electron charge, V_{act} the active region volume, v_g the group velocity, β the spontaneous emission coefficient, Γ the longitudinal confinement factor, τ_p the photon lifetime, α_H is the phase-amplitude coupling factor referred also as Henry Factor, a_0 the differential gain coefficient, ϵ the gain compression factor, N_{tr} the transparency carrier density, A is the Shockly-Read-Hall non-radiative recombination coefficient, B the radiative recombination coefficient, C the Auger non-radiative recombination coefficient, and G the optical gain.

Steady-state analysis of rate equations are used to determine some VCSELs parameters, such as threshold current and steady-state carrier densities, under constant current injection. For this, time derivatives are set to zero ($d/dt = 0$) and different bias current conditions are considered.

The small-signal analysis gives information about VCSEL dynamical behavior under current modulation. For an operation well above the threshold, the resonance frequency f_R can be expressed as a function of the injected current I_{bias} as [40]:

$$f_R = \frac{1}{2\pi} \sqrt{\frac{\eta_i v_g \Gamma a_0}{qV_{act}}} \sqrt{I_{bias} - I_{th}}, \quad (4)$$

where Γ is the longitudinal confinement factor and I_{th} the threshold current.

The active region of a laser can be modeled through the equivalent electrical circuit [41] shown in Fig. 2. This model has been used in previous works for modeling 850-nm VCSELs [42,43] and long-wavelength VCSELs [34]. The parallel circuit $R_j C_j$ symbolizes the quantum wells, the series circuit $R_0 L_0$ represents the losses and storage of photons in the optical cavity, and H is the transimpedance of the current-controlled voltage-source equivalent to an optical power. Each electrical component is expressed in terms of the intrinsic VCSEL parameters after applying Kirchhoff's law and using the linearized carrier and photon rate equations.

The turn-on delay t_D is the delay between the application of a current pulse and the beginning of the corresponding optical pulse produced by the laser. The TOD measurement procedure consists of applying an electrical pulse to the VCSEL, with I_{ON} and I_{OFF} the high and low-level current, when it is pre-biased below its threshold current I_{th} [44]. The TOD is dominated by the

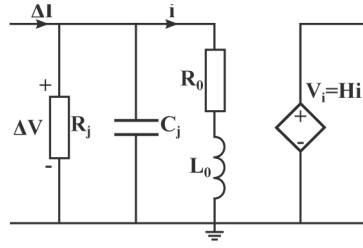


Fig. 2. Equivalent electrical scheme of the active region [41].

carrier lifetime τ_N and is expressed as [45]:

$$t_D = \tau_N \cdot \ln \left(\frac{I_{ON} - I_{OFF}}{I_{ON} - I_{th}} \right). \quad (5)$$

The experimental setup used to measure the TOD is described by Bacou *et al.* in [34]. A calibration process is required for removing the additional delays produced by the electrical and optical connections. In order to determine the carrier lifetime, several TOD measurements are performed to guarantee high precision. Therefore, for each bias current ($0 < I_{bias} < I_{th}$), the high pulse level I_{ON} is modified at different values. Figure 3 shows the TOD measurements against the natural logarithm expressed in Eq. (5). Once a linear polynomial fitting is applied, the carrier lifetime can be estimated. Furthermore, we can estimate the laser's transient relaxation frequency at different bias currents using the same setup. When $I_{bias} = 6$ mA, the relaxation frequency is 2.1 GHz.

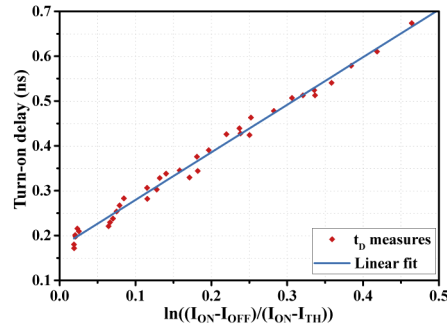


Fig. 3. Turn-on delay measurements at different I_{bias} values.

Generally, the measurements of the intrinsic frequency response of laser diodes include the modulation response of packaging, chip parasitics, and measurement setup elements. In the case of our packaged VCSEL, the main contributions are the TO-56 can leads and the wire bondings.

The VCSEL bandwidth is acquired by measuring the parameter S_{21} for bias currents from 2 to 7 mA. Figure 4(a) shows the S_{21} parameter measurements after extracting the photodetector frequency response and normalizing the data to the magnitude at low frequencies. There is a 3-dB bandwidth improvement of 2 GHz (from 2.7 to 4.7 GHz) when the current ranges from 2 to 7 mA.

In all cases, the frequency response presents a bump after reaching the resonance frequency that decreases with a slope greater than -60 dB/dec. This phenomenon is produced by the driver circuits, connections, and packaging employed during the measurements. Despite the frequency response degradation, the resonance frequency f_R for each current is certainly identifiable.

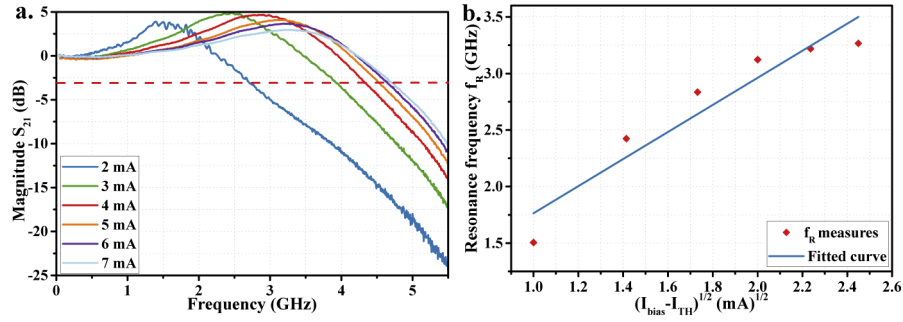


Fig. 4. a. S_{21} measurement at different I_{bias} . **b.** Squared resonance frequency versus square root of $I_{bias} - I_{th}$.

Figure 4(b) represents the f_R evolution versus the square root of the difference between I_{bias} and I_{th} (see Eq. (4)). The differential gain coefficient estimation using the fitted data is limited by the frequency resonance reduction caused by active region heating at bias currents higher than 5 mA.

Additional VCSEL parameters are estimated by the extraction procedure described in [34] and the simulation of the equivalent circuit model of the optical cavity (including the DBR reflectors).

The VCSEL frequency response is simulated in Advanced Design System (ADS) using the electrical parameters of the active region and an electrical access model. Figure 5(a) depicts the measured and simulated frequency responses when the bias current is 2, 4, and 6 mA. In all cases, the electric model shows a good agreement with the measurements.

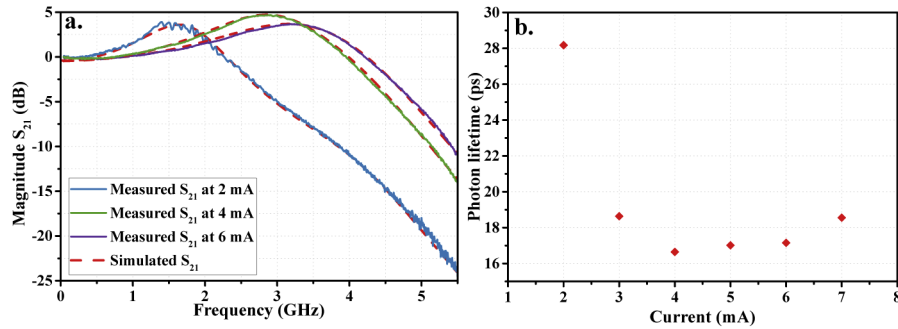


Fig. 5. a. Measured and simulated VCSEL frequency response at different bias currents. **b.** Photon lifetime evolution as a function of bias current.

Once VCSEL cavity parameters have been established, the photon density, gain compression factor, transparency carrier density, and photon lifetime are obtained. Due to the absorption losses variations produced by the electron-hole injection at different bias currents [46], the photon lifetime varies as shown in Fig. 5(b). The estimated photon lifetime for bias currents higher than 2 mA is $\tau_P = 18.47$ ps. In [31] the authors found $\tau_P = 19$ ps for the same pigtailed RayCan VCSEL, whereas for an LW-VCSEL manufactured by Vertilas the reported lifetime is 14 ps [17].

The intrinsic parameters extracted for a C-band VCSEL are summarized in Table 1.

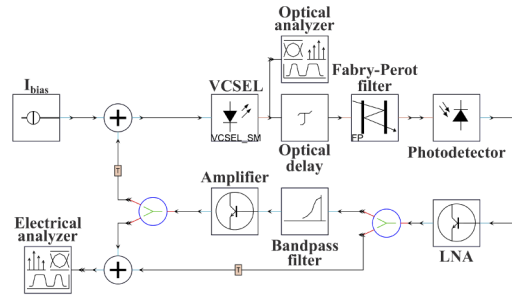
3.2. SVOFC simulations

The C-band SVOFC is simulated in VPIphotonics Design SuiteTM using the schematic shown in Fig. 6. The C-band VCSEL is modeled by a single-mode rate equation-based VCSEL model configured according to the intrinsic parameters listed in Table 1. This VCSEL model includes a temperature-dependent pump current offset to describe the self-heating dynamics inside the laser

Table 1. C-band VCSEL intrinsic parameters extracted

Symbol	Parameter	Value	Units	Source
I_{th}	Threshold current	0.90	mA	Measured
τ_N	Carrier lifetime	1.06	ns	Measured
η_i	Internal quantum efficiency	0.90		Assumed
N_{th}	Threshold carrier density	3.82×10^{18}	cm^{-3}	Measured
A	Non-radiative recombination coefficient	2.10×10^7	s^{-1}	[47]
B	Radiative recombination coefficient	0.90×10^{-10}	$cm^3 s^{-1}$	[47]
C	Auger recombination coefficient	3.96×10^{-29}	$cm^6 s^{-1}$	Measured
v_g	Group velocity	7.50×10^9	cms^{-1}	[48]
Γ	Longitudinal confinement factor	0.032		[48]
a_0	Differential gain coefficient	2.85×10^{-16}	cm^2	Measured
ϵ	Gain compression factor	1.57×10^{-17}	cm^3	Measured
N_{tr}	Transparency carrier density	2.95×10^{18}	cm^{-3}	Measured
τ_P	Photon lifetime	18.47	ps	Measured
α_H	Linewidth enhancement factor	3.06		Measured

cavity associated with the thermal leakage current, e.g., thermally dependent threshold current and thermal frequency shift. Additionally, the laser frequency chirp is included into the model through a complex gain function and the linewidth enhancement factor (α_H or Henry's factor). This function relates the change of the material refractive index caused by carrier density and material gain fluctuations. The optical fiber consists of an optical delay and a transmission mode Fabry-Perot (FP) filter responsible for the free spectral range. The non-linear effects of the optical fiber are neglected. The photodetection process is performed with a PIN type photodetector, which includes thermal and shot noise. The amplification stage is divided into two: a first low noise amplifier (LNA) responsible for establishing the white noise level and the second amplifier of higher gain for establishing the power level required to guarantee the GS condition. Finally, the filter is modeled with a fourth-order Bessel filter centered at the desired fundamental frequency.

**Fig. 6.** VPI schematic for simulating the C-band SVOFC.

For all simulation cases, the C-band VCSEL is biased at the same current $I_{bias} = 6$ mA. Two fundamental frequencies f_0 are selected: $f_0 = 1.25$ GHz and $f_0 = 2.5$ GHz. The impact of the optical delay line length on the generated signals is adjusted through the FSR of the FP filter and the optical delay time τ_o . For $L = 1$ km, the simulated FSR is 200 kHz and $\tau_o = 5$ μs , and for $L = 2$ km, the simulated values are $FSR = 100$ kHz and $\tau_o = 10$ μs . The simulation boundary conditions are set to aperiodic because the laser module generates several blocks (sampled signal) for each simulation run. The aperiodic condition guarantees update of visualizers for each data

block. To achieve the GS regime when $FSR = 200$ kHz, it is necessary to compensate for the additional optical losses caused by the FP filter. These losses are induced by the change of the passband width (directly related to FSR) and the temporal analysis of the optical signal using a windowed finite impulse response filter (FIR) for aperiodic conditions. Consequently, the total electrical gain for $FSR = 200$ kHz is 3 dB higher than for $FSR = 100$ kHz.

The resulting optical frequency combs for $f_0 = 1.25$ GHz are shown in Fig. 7. In both cases, the spectrum is asymmetrical around the primary tone with the highest optical power due to the effect of negative frequency chirp. The distance between the secondary tones corresponds well to the fundamental frequency. The spectral width at 30 dB from the primary tone is 21.2 GHz and 23.5 GHz for $FSR = 200$ and $FSR = 100$ kHz, respectively. Considering the spectral asymmetry and the decreasing power of the secondary tones, the flatness of the two optical frequency combs is low (0.58 on average). Figure 7 insets show the effect of the resonant cavity on the modulated optical signal. In each case, a frequency sub-comb is observed with a distance between tones equal to the FSR value. This recognition can only be performed in a simulation environment because there are no commercially available optical spectrum analyzers with a small resolution.

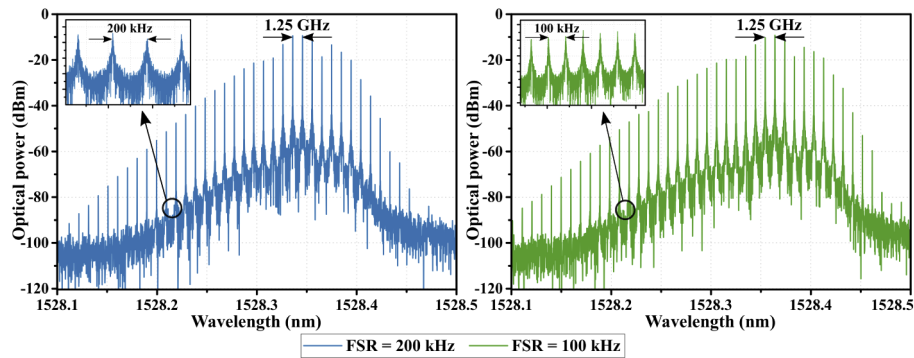


Fig. 7. Simulated optical spectra of the C-band SVOFC at 1.25 GHz using $FSR = 200$ kHz and $FSR = 100$ kHz.

When $f_0 = 2.5$ GHz and $FSR = 100$ kHz, the generated OFC shown in Fig. 8 remains asymmetrical but it is wider (63 GHz at 30 dB) and flatter (0.8) than the case of 1.25-GHz SVOFC. Consequently, and as demonstrated in [35], wider and flatter OFCs are obtained at modulation frequencies closer to the VCSEL resonance frequency ($f_R = 3.2$ GHz when $I_{bias} = 6$ mA).

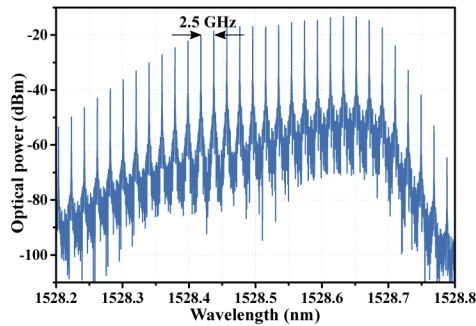


Fig. 8. Optical spectrum of the simulated C-band SVOFC at 2.5 GHz.

Finally, the fundamental frequency of the 1.25-GHz SVOFC is analyzed using its spectrum (Fig. 9(a)) and phase noise (Fig. 9(b)) for both FSR values. The electrical spectra consist of a power oscillation mode dominant over non-oscillating modes spaced according to the selected FSR. The power levels are -8.7 dBm and -5.2 dBm for $FSR = 200$ and $FSR = 100$ kHz, respectively. As expected, the phase noise at 10 kHz from the carrier is improved by 13 dB when the FSR passes from 200 kHz (-116 dBc/Hz) to 100 kHz (-129 dBc/Hz). Figure 9(b) shows that the white noise processes are at the same level due to the white noise contributed by the microwave amplifiers. The phase noise close-to-the-carrier can be determined more accurately by increasing the sample rate and the time window of the simulation.

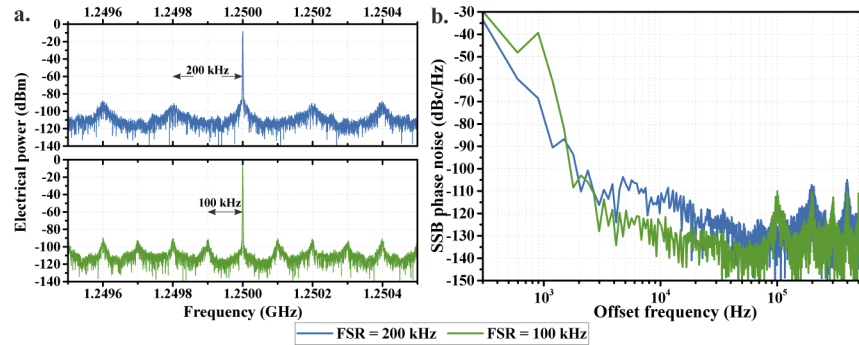


Fig. 9. **a.** Electrical spectra and **b.** simulated SSB phase noise of the C-band SVOFC at 1.25 GHz.

4. SVOFC experimental validation

4.1. OFC characterization

The SVOFC is implemented according to the architecture depicted in Fig. 1. VCSEL temperature was not directly controlled but all experimental implementations and measurements were performed in a temperature-controlled clean room at 23 °C. The optical coupler (F-CPL Newport) allows for very precise adjustment of the coupling ratio from 0 to 100%. The resonant cavity consists of different single-mode SMF-28e+ optical fiber lengths. A photodetector with 17 GHz bandwidth and 0.94 A/W responsivity is used. The microwave amplifier has a 38-dB flat gain and a wide band from 0.5 to 18 GHz. Considering the VCSEL bandwidth and the resonance frequency, two cavity filters tuned at 1.25 GHz and 2.5 GHz are included. Given the polarization properties of the VCSEL under the GS regime, two orthogonally polarized OFCs are produced for each implementation [16,17]. However, the OFCs discussed in this section result from the combination of the two polarized OFCs and are characterized with a high resolution (10 MHz) Brillouin optical spectrum analyzer (Aragon Photonics BOSA 400). The spectral quality of the fundamental frequency is measured by an electrical spectrum analyzer ESA (R&S FSW50).

The OFC generated by the C-band SVOFC at 1.25 GHz using a fixed fiber length ($L = 1$ km) and different bias conditions is presented in Fig. 10. As well as the simulation (Fig. 7), the experimental spectra have an asymmetric envelope with a marked decrease at higher wavelengths (right side) and suppressed tones. This spectrum asymmetry is induced by the frequency chirp of the large-signal modulation (amplitude-phase coupling of the laser). Measured spectra include fewer tones than the simulation because the dynamic range of the optical spectrum analyzer used (about 80 dB) is lower than the one used during the simulation. Tone suppression is induced by the effect of the frequency modulation (FM) produced either by the effect of carrier density modulation or by temperature variations [49]. The VCSEL module in VPI does not consider the FM modulation effect, and consequently, the simulated spectra do not include mode suppression.

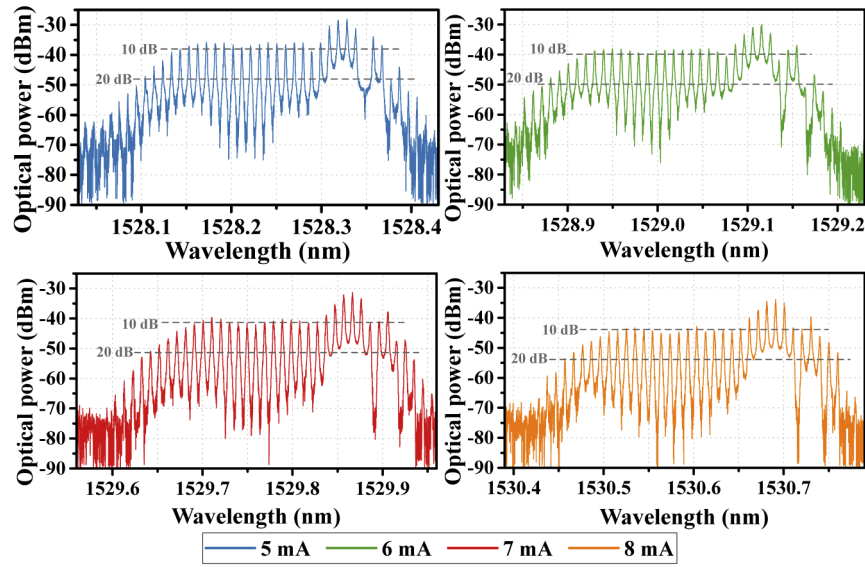


Fig. 10. Optical spectra of the C-band SVOFC at 1.25 GHz and different I_{bias} currents.

The optical spectra width measured at 30 dB from the highest power is 42 GHz (~ 0.33 nm) for all the implementations. This spectral width is constant since the electrical power used to modulate the VCSEL varies slightly. For lower electrical powers, adjusted through a variable electrical attenuator, the spectral width of the frequency comb decreases, whereas for higher powers, the width is enlarged until it reaches the maximum. Although a wider optical frequency comb may be desired, high electrical powers can lead the SVOFC into a frequency doubling status [50], deteriorating system performance in the optical and electrical domains.

The frequency combs are characterized according to their flatness at 20 dB, and the 10 dB and 20 dB spectral width (Δf_{10} and Δf_{20}). Table 2 summarizes the results of the C-band SVOFC where $L = 1$ km. The OFC flatness deteriorates from 0.75 to 0.42 as an effect of the increasing electrical power inside the loop caused by the bias current augmentation from 5 mA to 8 mA. This deterioration is attributed to the “vanishing” of secondary tones in the middle of the comb profile. The Δf_{10} and Δf_{20} do not vary representatively because the tones at the edges are conserved. Even if 0.75 flatness is achieved, the SVOFC performance at 1.25 GHz is limited by the effect of the negative frequency chirp.

Table 2. Summary C-band SVOFC at 1.25 GHz and $L = 1$ km.

I_{bias} (mA)	# tones at 10 dB	# tones at 20 dB	Flatness	Δf_{10} (GHz)	Δf_{20} (GHz)
5	21	28	0.75	27.47	36.22
6	21	29	0.72	28.82	37.55
7	13	30	0.43	26.30	36.19
8	13	31	0.42	26.23	38.78

Figure 11 shows the OFC when the band-pass filter is centered at 2.5 GHz, the bias current is fixed at 6 mA, and the optical fiber length is modified. Although the comb envelope remains asymmetrical, the mid-tones are not suppressed. The spectral width is 50 GHz measured at 30 dB from the peak power for all fiber lengths. This value is constant because the electrical modulation conditions are guaranteed to be the same. The non-suppression and the modulation conditions result in a flatter profile in comparison to the profile obtained for the C-band SVOFC

at 1.25 GHz. Table 3 condenses the performance of the OFCs generated. The flatness in all four cases is higher than 0.84, exceeding the performance of the C-band SVOFC at 1.25 GHz (Table 2). The highest difference between the Δf_{10} spectral widths is 2.5 GHz, whereas for Δf_{20} it is 5 GHz. This means that the highest variation is given by the occurrence of two supplementary tones where $L = 1$ km and $L = 3$ km. Additionally, the carrier-to-noise (CNR) measured in a 10 dB span is higher than 25 dB in all cases, whereas for the 1.25-GHz SVOFC, several tones do not exceed a CNR of 15 dB (see Fig. 10).

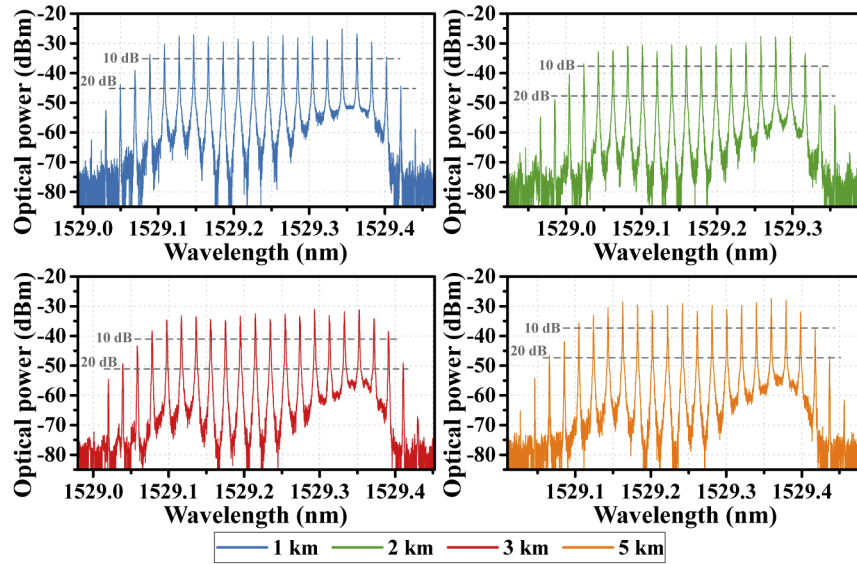


Fig. 11. Optical spectra of the C-band SVOFC at 2.5 GHz and different fiber lengths.

Table 3. Summary C-band SVOFC at 2.5 GHz.

Fiber length (km)	# tones at 10 dB	# tones at 20 dB	Flatness	Δf_{10} (GHz)	Δf_{20} (GHz)
1	17	20	0.85	40.18	47.60
2	16	18	0.89	37.60	42.57
3	17	20	0.85	40.12	47.61
5	16	19	0.84	37.63	45.12

The SVOFC performance at 2.5 GHz is remarkably close to that achieved by a gain-switched VCSEL using only a DC current source and a signal generator [16]. In this case, the VCSEL is modulated at 5 GHz, and 24 and 27 tones are generated at 10 dB and 20 dB, respectively. Therefore, the flatness is 0.89 and corresponds to the SVOFC flatness where $L = 2$ km. Similarly, in [9], the authors use a discrete mode laser (DML) gain-switched at 5 GHz to obtain a flatness of 0.87 when 13 and 15 tones are generated at 10 and 20 dB offset, respectively. In both cases, the Δf_{10} and Δf_{20} spectral widths are higher than those generated by the SVOFC due to the higher modulating frequency and the physical differences of the lasers.

4.2. Microwave signal characterization

As was demonstrated through the SVOFC simulation, the generated microwave signal is composed of the main mode at frequency f_0 and several equally spaced non-oscillating modes. The side mode suppression ratio (SMSR) measured between the main mode and the immediately adjacent

non-oscillating mode for all the implementations presented in this document is higher than 50 dB. The spectral purity of the extracted electrical signal at 1.25 GHz is determined by measuring the phase noise. In order to verify the impact of optical fiber dispersion, the SVOFC is also implemented using an O-band VCSEL and two optical fiber lengths. Figure 12 shows the phase noise of the C-band and O-band SVOFC for $L = 1$ km and $L = 5$ km. In the case of $L = 1$ km (Fig. 12(a)), the curves overlap over most of the observed frequency range, and the phase noise at 10 kHz from the carrier is -115 dBc/Hz. This curve superposition shows that the optical fiber dispersion (zero in O-band) does not impact the SVOFC phase noise behavior. The four slopes illustrated in Fig. 12(a) correspond to four noise processes produced by additive and multiplicative noise contributed by the system components. From right to left, the white phase noise is the first process and is governed by the white noise of the microwave amplifier (if the other noise source contributions are lower, such as the VCSEL RIN at the oscillation frequency). In this same region, the non-oscillating modes are equally spaced at 186 kHz and are produced by the Fabry-Pérot effect of the optical fiber. With a -20 dB/dec slope, the white frequency noise process is caused by the Leeson effect on the white noise of the microwave amplifier. The phase noise curve is followed by a noise process with a slope of -25 dBc/Hz, caused by multiplicative noises (e.g., the VCSEL frequency noise and the VCSEL RIN at low frequencies) and the Rayleigh scattering contribution. The last process is the Flicker frequency noise and results from the Leeson effect on the amplifier flicker noise at frequencies below its corner frequency f_c .

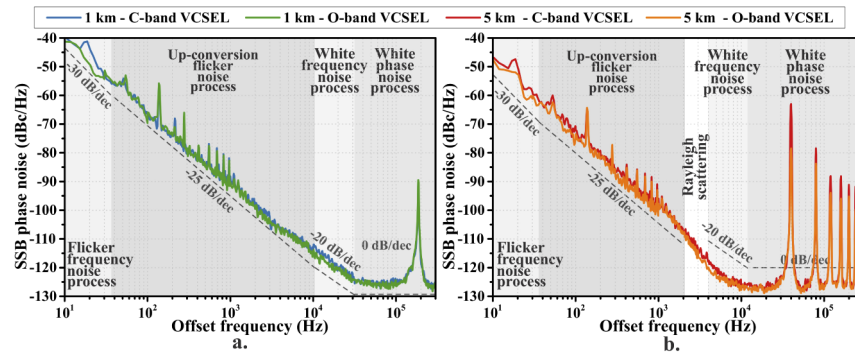


Fig. 12. Phase noise curves of the fundamental frequency at 1.25 GHz for **a.** $L = 1$ km, **b.** $L = 5$ km.

In the case of $L = 5$ km, Fig. 12(b), the phase noise is improved by about 12 dB as an effect of the quality factor Q of the resonant cavity. Thus, the phase noise at 10 kHz from the carrier is -126 dBc/Hz and -127 dBc/Hz for the C-band SVOFC and O-band SVOFC, respectively. The non-oscillating modes are closer than in the previous case due to the FSR reduction to 79 kHz (increased optical delay), resulting in higher RMS phase jitter. The same four noise processes are identified in the curves. Nevertheless, between 2 and 4 kHz, there is a pronounced transition generated by the higher Rayleigh scattering effect in long optical fibers.

5. Conclusions

We have presented and experimentally demonstrated the first closed-loop system for optical frequency comb generation using a modulated VCSEL in gain-switching condition. In order to simulate the SVOFC system, we applied an intrinsic parameter extraction process based on the steady-state and small-signal analysis of the VCSEL rate equations. The process included dynamic measurements and electrical model simulations of the electrical access and VCSEL cavity.

Through C-band SVOFC simulation and implementation, we demonstrated that the performance of the optical frequency comb generated with the SVOFC is related to the bias current, the modulating electrical power, and the repetition frequency. For frequencies far from the VCSEL resonance frequency f_R , the OFC envelope is less flat owing to the tone suppression during the first 10 dB span (8 suppressed tones). In contrast, for closer frequencies, the spectral width of the envelope is constant and its profile is flatter. It is worth pointing out the importance of controlling the electrical conditions inside the loop to guarantee better performance. Hence, when the polarization current increases, the modulating electrical power must increase to deplete the carriers and enhance the photon absorption in the cavity. A wider comb is obtained by increasing the electrical loop power. After reaching the broadest spectral width, non-linear effects appear, such as the frequency doubling operation. These effects must be minimized to avoid deterioration of the electrical SVOFC performance.

The flatness of the OFC generated with our system is close to the one achieved by other authors applying the GS technique to VCSEL and DML lasers. The huge advantage of our SVOFC generator is the ability to adjust the OFC shape by modifying the modulating electrical power through the variable electrical attenuator, the variable ratio optical coupler, and the bias current. The fundamental frequency f_0 can be modified by including an adjustable bandpass filter in the loop, according to the laser frequency response and the amplifier gain and bandwidth. Given the characteristics of our system, the filter can cover the frequency range from 1 GHz to 5 GHz. A higher fundamental frequency than the one presented in this work can be achieved by using commercially available C-band on-chip VCSELs with bandwidths above 10 GHz in order to eliminate the electrical access constraint and produce tones at higher frequencies.

A temperature control can be applied to the VCSEL in order to reduce the thermal effects inside the optical cavity, such as wavelength deviation. Additionally, a detailed analysis of two orthogonally polarized OFCs must be carried out to determine the electrical conditions that allow a wider combined OFC.

Through some technical modifications, the SVOFC architecture can be applied to the generation of low-noise microwave harmonics at frequencies higher than 10 GHz. Some results on this matter are in the process of publication. Similarly, the width and spacing of OFC tones can be improved and used in sensing applications with fiber Bragg grating sensors, and the optical pulses generated through the GS regime at higher repetition rates can be exploited for optical data pulse shaping.

We also showed that the phase noise far-from-the-carrier of the electrical signal generated at f_0 depends strongly on the optical fiber length and the white noise contributed by the microwave amplifier. Thus, if the electrical conditions of the loop are guaranteed, the phase noise remains constant.

Funding

Departmental Government of Nariño (BPIN 2013000100092); Departamento Administrativo de Ciencia, Tecnología e Innovación (COLCIENCIAS) (M301PR03F18); Ministère de l'Éducation Nationale, de l'Enseignement Supérieur et de la Recherche (C17P01); Fondation ISAE-SUPAERO.

Disclosures

The authors declare no conflicts of interest.

References

1. B. Jerez, P. Martín-Mateos, E. Prior, C. de Dios, and P. Acedo, "Dual optical frequency comb architecture with capabilities from visible to mid-infrared," *Opt. Express* **24**(13), 14986–14994 (2016).
2. I. Coddington, N. Newbury, and W. Swann, "Dual-comb spectroscopy," *Optica* **3**(4), 414–426 (2016).

3. A. R. Criado, C. de Dios, E. Prior, G. H. Döhler, S. Preu, S. Malzer, H. Lu, A. C. Gossard, and P. Acedo, "Continuous-Wave Sub-THz Photonic Generation With Ultra-Narrow Linewidth, Ultra-High Resolution, Full Frequency Range Coverage and High Long-Term Frequency Stability," *IEEE Trans. Terahertz Sci. Technol.* **3**(4), 461–471 (2013).
4. I. Coddington, W. Swann, L. Nenadovic, and N. Newbury, "Rapid and precise absolute distance measurements at long range," *Nat. Photonics* **3**(6), 351–356 (2009).
5. M. Imran, P. M. Anandarajah, A. Kaszubowska-Anandarajah, N. Sambo, and L. Potí, "A Survey of Optical Carrier Generation Techniques for Terabit Capacity Elastic Optical Networks," *IEEE Commun. Surv. Tutorials* **20**(1), 211–263 (2018).
6. D. A. Poiana, J. A. García-Souto, J. E. Posada-Román, and P. Acedo, "Interrogation system with auto-calibration for fiber Bragg grating sensors using VCSEL based optical frequency comb generators," in *Proceedings of 2017 25th Optical Fiber Sensors Conference (OFS)*, (IEEE, 2017), pp. 1–4.
7. A. E. Akosman and M. Y. Sander, "Dual comb generation from a mode-locked fiber laser with orthogonally polarized interlaced pulses," *Opt. Express* **25**(16), 18592–18602 (2017).
8. W. T. Wang, J. G. Liu, W. H. Sun, W. Chen, and N. H. Zhu, "Multi-band local microwave signal generation based on an optical frequency comb generator," *Opt. Commun.* **338**, 90–94 (2015).
9. A. Rosado, A. Pérez-Serrano, J. M. G. Tijero, Á. Valle, L. Pesquera, and I. Esquivias, "Experimental study of optical frequency comb generation in gain-switched semiconductor lasers," *Opt. Laser Technol.* **108**, 542–550 (2018).
10. A. Quirce, C. de Dios, A. Valle, and P. Acedo, "VCSEL-Based Optical Frequency Combs Expansion Induced by Polarized Optical Injection," *IEEE J. Sel. Top. Quantum Electron.* **25**(6), 1–9 (2019).
11. S. Tarucha and K. Otsuka, "Response of semiconductor laser to deep sinusoidal injection current modulation," *IEEE J. Quantum Electron.* **17**(5), 810–816 (1981).
12. A. Delmade, M. Krstić, C. Browning, J. Crnjanski, D. Gvozdić, and L. Barry, "Power efficient optical frequency comb generation using laser gain switching and dual-drive Mach-Zehnder modulator," *Opt. Express* **27**(17), 24135–24146 (2019).
13. A. Rosado, A. Pérez-Serrano, J. M. G. Tijero, Á. Valle, L. Pesquera, and I. Esquivias, "Enhanced optical frequency comb generation by pulsed gain-switching of optically injected semiconductor lasers," *Opt. Express* **27**(6), 9155–9163 (2019).
14. E. Prior, C. de Dios, Á. R. Criado, M. Ortsiefer, P. Meissner, and P. Acedo, "Expansion of VCSEL-Based Optical Frequency Combs in the Sub-THz Span: Comparison of Non-Linear Techniques," *J. Lightwave Technol.* **34**(17), 4135–4142 (2016).
15. A. Criado, C. de Dios Fernandez, E. P. Cano, M. Ortsiefer, P. Meissner, and P. Acedo, "VCSEL-Based Optical Frequency Combs: Toward Efficient Single-Device Comb Generation," *IEEE Photonics Technol. Lett.* **25**(20), 1981–1984 (2013).
16. E. Prior, C. De Dios, M. Ortsiefer, P. Meissner, and P. Acedo, "Understanding VCSEL-Based Gain Switching Optical Frequency Combs: Experimental Study of Polarization Dynamics," *J. Lightwave Technol.* **33**(22), 4572–4579 (2015).
17. A. Quirce, C. de Dios, A. Valle, L. Pesquera, and P. Acedo, "Polarization Dynamics in VCSEL-Based Gain Switching Optical Frequency Combs," *J. Lightwave Technol.* **36**(10), 1798–1806 (2018).
18. Q. Cheng, M. Bahadori, M. Glick, S. Rumley, and K. Bergman, "Recent advances in optical technologies for data centers: a review," *Optica* **5**(11), 1354–1370 (2018).
19. J. M. Castro, R. Pimpinella, B. Kose, P. Huang, B. Lane, K. Szczerba, P. Westbergh, T. Lengyel, J. S. Gustavsson, A. Larsson, and P. A. Andrekson, "Investigation of 60 Gb/s 4-PAM Using an 850 nm VCSEL and Multimode Fiber," *J. Lightwave Technol.* **34**(16), 3825–3836 (2016).
20. R. Puerta, M. Agustin, L. Chorchos, J. Toński, J. R. Kropp, N. Ledentsov, V. A. Shchukin, N. N. Ledentsov, R. Henker, I. T. Monroy, J. J. V. Olmos, and J. P. Turkiewicz, "Effective 100 Gb/s IM/DD 850-nm Multi- and Single-Mode VCSEL Transmission Through OM4 MMF," *J. Lightwave Technol.* **35**(3), 423–429 (2017).
21. F. Karinou, C. Prodaniuc, N. Stojanovic, M. Ortsiefer, A. Daly, R. Hohenleitner, B. Kögel, and C. Neumeyr, "Directly PAM-4 Modulated 1530-nm VCSEL Enabling 56 Gb/s/λ Data-Center Interconnects," *IEEE Photonics Technol. Lett.* **27**(17), 1872–1875 (2015).
22. P. Pepeljugoski, J. Lin, J. Gamelin, M. Hong, and K. Y. Lau, "Ultralow timing jitter in electrically gain-switched vertical cavity surface emitting lasers," *Appl. Phys. Lett.* **62**(14), 1588–1590 (1993).
23. G. Hasnain, J. M. Wiesenfeld, T. C. Damen, J. Shah, J. D. Wynn, Y. H. Wang, and A. Y. Cho, "Electrically gain-switched vertical-cavity surface-emitting lasers," *IEEE Photonics Technol. Lett.* **4**(1), 6–9 (1992).
24. K. Koizumi, M. Yoshida, and M. Nakazawa, "10-GHz 11.5-ps Pulse Generation From a Single-Mode Gain-Switched InGaAs VCSEL at 1.1 μm," *IEEE Photonics Technol. Lett.* **21**(22), 1704–1706 (2009).
25. A. Consoli, J. M. Noriega, A. Valle, L. Pesquera, I. Esquivias, and F. J. López-Hernández, "Optical injection-induced timing jitter reduction in gain-switched single-mode vertical-cavity surface-emitting lasers," *Proc. SPIE* **7720**, 77200H (2010).
26. J. Dai, X. Xu, Z. Wu, Y. Dai, F. Yin, Y. Zhou, J. Li, and K. Xu, "Self-oscillating optical frequency comb generator based on an optoelectronic oscillator employing cascaded modulators," *Opt. Express* **23**(23), 30014–30019 (2015).
27. X. Xiao, S. Li, Z. Xie, S. Peng, D. Wu, X. Xue, X. Zheng, and B. Zhou, "Photonic harmonic up-converter based on a self-oscillating optical frequency comb using a DP-DPMZM," *Opt. Commun.* **413**, 48–53 (2018).
28. J. Liu, B. Zheng, and C. Shu, "Self-Oscillating Optical Frequency Comb Based on a Raman-Pumped Brillouin Optoelectronic Oscillator," *IEEE Photonics Technol. Lett.* **29**(12), 1003–1006 (2017).

29. J. Yan and A. Liang, "Self-oscillating frequency comb generation with a stimulated Brillouin scattering based optoelectronic oscillator," *Opt. Fiber Technol.* **46**, 68–71 (2018).
30. A. Villafranca, J. Lasobras, J. A. Lazaro, and I. Garcés, "Characterization of the Main Semiconductor Laser Static and Dynamic Working Parameters From CW Optical Spectrum Measurements," *IEEE J. Quantum Electron.* **43**(2), 116–122 (2007).
31. P. Pérez, A. Valle, I. Noriega, and L. Pesquera, "Measurement of the Intrinsic Parameters of Single-Mode VCSELs," *J. Lightwave Technol.* **32**(8), 1601–1607 (2014).
32. M. Bruenstener and G. C. Papen, "Extraction of VCSEL rate-equation parameters for low-bias system simulation," *IEEE J. Sel. Top. Quantum Electron.* **5**(3), 487–494 (1999).
33. J. Gao, "High Frequency Modeling and Parameter Extraction for Vertical-Cavity Surface Emitting Lasers," *J. Lightwave Technol.* **30**(11), 1757–1763 (2012).
34. A. Bacou, A. Hayat, V. Iakovlev, A. Syrbu, A. Rissons, J. C. Mollier, and E. Kapon, "Electrical modeling of long-wavelength VCSELs for intrinsic parameters extraction," *IEEE J. Quantum Electron.* **46**(3), 313–322 (2010).
35. A. Rosado, A. Pérez-Serrano, J. M. G. Tijero, A. V. Gutierrez, L. Pesquera, and I. Esquivias, "Numerical and Experimental Analysis of Optical Frequency Comb Generation in Gain-Switched Semiconductor Lasers," *IEEE J. Quantum Electron.* **55**(6), 1–12 (2019).
36. A. Consoli, I. Esquivias, F. J. Lopez Hernandez, J. Mulet, and S. Balle, "Characterization of Gain-Switched Pulses From 1.55- μ m VCSEL," *IEEE Photonics Technol. Lett.* **22**(11), 772–774 (2010).
37. A. Consoli, "Short Pulse Generation From Semiconductor Lasers: Characterization, Modeling And Applications," Ph.D. thesis, Universidad Politécnica de Madrid (2011).
38. M. Park, O. Kwon, W. Han, K. Lee, S. Park, and B. Yoo, "All-epitaxial InAlGaAs-InP VCSELs in the 1.3-1.6- μ m wavelength range for CWDM band applications," *IEEE Photonics Technol. Lett.* **18**(16), 1717–1719 (2006).
39. C. J. O'Brien, M. L. Majewski, and A. D. Rakic, "A Critical Comparison of High-Speed VCSEL Characterization Techniques," *J. Lightwave Technol.* **25**(2), 597–605 (2007).
40. L. A. Coldren and S. W. Corzine, *Diode Lasers and Photonic Integrated Circuits* (Wiley, 1995).
41. R. Tucker and I. Kaminow, "High-frequency characteristics of directly modulated InGaAsP ridge waveguide and buried heterostructure lasers," *J. Lightwave Technol.* **2**(4), 385–393 (1984).
42. A. Rissons, "Caractérisation et modélisation optoélectronique de diodes laser à cavité verticale émettant par la surface (VCSEL)," Ph.D. thesis, École National Supérieure de l'Aéronautique et de l'Espace (2003).
43. J. Perchoux, "Caractérisation et modélisation du bruit d'intensité de VCSELs (Al- GaAs) et de son influence sur le bruit de phase des liaisons opto-hyperfréquences," Ph.D. thesis, École National Supérieure de l'Aéronautique et de l'Espace (2005).
44. T. Fukushima, A. Kasukawa, M. Iwase, T. Namegaya, and M. Shibata, "Compressively strained 1.3 μ m InAsP/InP and GaInAsP/InP multiple quantum well lasers for high-speed parallel data transmission systems," *IEEE J. Quantum Electron.* **29**(6), 1536–1543 (1993).
45. D. Wiedenmann, R. King, C. Jung, R. Jäger, R. Michalzik, P. Schnitzer, M. Kicherer, and K. J. Ebeling, "Design and analysis of single-mode oxidized VCSELs for high-speed optical interconnects," *IEEE J. Sel. Top. Quantum Electron.* **5**(3), 503–511 (1999).
46. B. R. Bennett, R. A. Soref, and J. A. Del Alamo, "Carrier-induced change in refractive index of InP, GaAs and InGaAsP," *IEEE J. Quantum Electron.* **26**(1), 113–122 (1990).
47. A. Consoli, J. Arias, J. M. Tijero, F. J. L. Hernández, and I. Esquivias, "Electrical characterization of long wavelength VCSELs with tunnel junction," *Proc. SPIE* **7952**, 79520C (2011).
48. A. Bacou, "Caractérisation et modélisation optoélectronique de VCSELs à grande longueur d'onde pour sous-ensembles optiques intégrés," Ph.D. thesis, Université de Toulouse (2008).
49. S. Kobayashi, Y. Yamamoto, M. Ito, and T. Kimura, "Direct frequency modulation in AlGaAs semiconductor lasers," *IEEE J. Quantum Electron.* **18**(4), 582–595 (1982).
50. W. Jian, Q. Ji-Fang, and L. Jin-Tong, "Period-Doubling in 10 GHz Gain-Switched DFB Laser Diode," *Chin. Phys. Lett.* **24**(10), 2852–2854 (2007).